Nanoscale phosphoinositide distribution on cell membranes of mouse cerebellar neurons

Abbreviated title

Nanoscale phosphoinositide distribution in neuron

Author names and affiliations

Kohgaku Eguchi[1*] and Ryuichi Shigemoto[1*]

[1]Institute of Science and Technology Austria (ISTA), Am Campus 1, 3400 Klosterneuburg, Austria

[*]For correspondence: kohgaku.eguchi@ist.ac.at (KE); ryuichi.shigemoto@ist.ac.at (RS)

Number of pages: 48

Number of figures: 7

Number of words: abstract: 170, introduction: 595, discussion: 1,389

Conflict of Interest statement

The authors declare no competing financial interests.

Acknowledgments

We would like to thank Nicoleta Condruz (IST Austria, Klosterneuburg, Austria) for technical assistance with sample preparation; the Electron Microscopy Facility of IST Austria (Klosterneuburg, Austria) for technical support with EM works; Natalia Baranova (University of Vienna, Vienna, Austria) and Martin Loose (IST Austria, Klosterneuburg, Austria) for advice on liposome preparation; Yugo Fukazawa (University of Fukui, Fukui,

Japan) for comments. This work was financially supported by funding from the Institute of Science and Technology Austria, the European Union's Horizon 2020 research and innovation program under the Marie Skłodowska-Curie grant agreement No. 793482 (to KE), and the European Research Council (ERC) grant agreement No. 694539 (to RS).

Abstract

Phosphatidylinositol-4,5-bisphosphate (PI(4,5)P_2) plays an essential role in neuronal activities through interaction with various proteins involved in signaling at membranes. However, the distribution pattern of PI(4,5)P_2 and the co-clustering with these proteins on the neuronal cell membranes remain elusive at the electron microscopic level. In this study, we quantitatively investigated the nanoscale distribution of PI(4,5)P_2 on the neuronal cell membranes by SDS-digested freeze-fracture replica labeling with cryo-fixed mouse cerebellum. We demonstrate that PI(4,5)P_2 makes clusters with a mean size of ~ 1,000 nm^2 and these clusters show preferential accumulation in specific membrane compartments depending on cell types. Purkinje cell (PC) spines and granule cell (GC) presynaptic active zones are particularly rich in the PI(4,5)P_2 clusters. Furthermore, these clusters are extensively associated with clusters of $Ca_V2.1$ and GIRK3 throughout different membrane compartments of PCs, GCs, and molecular layer interneurons. In contrast, these clusters showed compartment-specific association with mGluR1α in PC spines. These results suggest that visualization of the nanoscale PI(4,5)P_2 distribution may provide insight into the physiological functions of PI(4,5)P_2 in neurons.

Introduction

Phosphoinositides (PIs) are minor components on the cytoplasmic side of eukaryotic cell membranes, but they play essential roles in a wide variety of cellular functions. In neuronal cells, each stereoisomer of PIs is distributed in different subcellular compartments (Haucke, 2005; Idevall-Hagren and De Camilli, 2015; Wenk and De Camilli, 2004): PI(4)P is enriched in the membrane of the Golgi apparatus and synaptic vesicles (SVs), PI(4,5)P_2 and PI(3,4,5)P_3 mainly exist in the plasma membrane, PI(3)P and PI(3,5)P_2 are selectively

concentrated on early and late endosomes, respectively. PIs contribute to various aspects of neuronal activity, such as synaptic transmission and maintenance of membrane excitability by regulating ion channels and intracellular signaling pathways. At chemical synapses, PIs regulate exo- and endocytosis of synaptic vesicles at the presynaptic sites (Lei et al., 2017; Martin, 2001; Posor et al., 2015; Ueda and Hayashi, 2013)Many proteins related to SV exo- and endocytosis have binding domains to one or several stereoisomers of PIs (Di Paolo and De Camilli, 2006; Falkenburger et al., 2010), indicating a potential role of PIs as an anchor for these presynaptic proteins to regulate their localization and dynamics during synaptic transmission. At the postsynaptic sites, PIs regulate the morphological plasticity of dendritic spines through actin remodeling (Lei et al., 2017; Martin, 2001; Posor et al., 2015; Ueda and Hayashi, 2013)during long-term potentiation (Lei et al., 2017; Martin, 2001; Posor et al., 2015; Ueda and Hayashi, 2013).

Although it is essential to know the distribution pattern of PIs and their association with signaling proteins at neuronal cell membranes to understand the roles of PIs in neuronal activities, it has been poorly investigated due to several technical issues in the conventional methods (Tsuji et al., 2019). Immunoelectron microscopy using anti-PI(4,5)P_2 antibody allows for observing the nanoscale PI(4,5)P_2 distribution on the cell membrane, but the use of aldehyde-fixed cell preparations has a potential issue because aldehydes cannot fix the lateral diffusion of most membrane lipids across the membrane (Tanaka et al., 2010). Fluorescent probes for PIs based on a PI-binding domain (PBD) of proteins have been developed to visualize PIs in living cells (Idevall-Hagren and De Camilli, 2015; Maekawa and Fairn, 2014). However, this method does not have sufficient spatial resolution to observe the nanoscale distribution of PIs in small compartments in neuronal cell membranes, such as presynaptic active zones (AZs) and postsynaptic densities (PSDs). In addition, the overexpressed PBD-based probes mask PIs and competitively interfere with their interactions

with proteins in the living cells (Suh and Hille, 2008).

To solve these issues and visualize the nanoscale distribution of PIs on cell membranes, sodium dodecyl sulfate-digested freeze-fracture replica labeling (SDS-FRL) combined with cryofixation has been utilized (Aktar et al., 2017; Cheng et al., 2014; Fujita et al., 2009; Ozato-Sakurai et al., 2011; Tsuji et al., 2019). This immunoelectron microscopic method enables nanoscale membrane phospholipid labeling by physically fixing membrane molecules without chemical fixation. In this study, we optimized this SDS-FRL method to acute mouse cerebellar slices and investigated the nanoscale distribution of PI(4,5)P_2 on neuronal cell membranes using recombinant GST-tagged pleckstrin homology (PH) domain of phospholipase Cδ1 (PLCδ1) as a specific probe for PI(4,5)P_2. This approach allowed us to quantitatively examine the numbers, densities, and distribution patterns of PI(4,5)P_2 on somatodendritic and axonal membranes, including post- and presynaptic sites in mouse cerebellar neurons. We show that PI(4,5)P_2 makes small clusters on neuronal membranes and specifically co-clusters with P/Q-type voltage-gated calcium channels, G-protein-coupled inwardly rectifying potassium channels, and metabotropic glutamate receptors in distinct membrane compartments, giving insights into the physiological functions of PI(4,5)P_2 in the regulation of neuronal excitability and neurotransmitter release.

Materials and Methods

Animals

Animal experiments were conducted in accordance with the guideline of the Institute of Science and Technology Austria (Animal license number: BMWFW-66.018/0012-WF/V/3b/2016). Mice were initially purchased from Jackson Laboratory (Bar Harbor, ME, USA) and were bred at the Preclinical Facility of IST Austria on 12:12 light-dark cycle with

access to food and water *ad libitum*. All experiments were performed in the light phase of the cycle. C57BL/6J (stock number 000664) mice of either sex at postnatal (P) 5-7 weeks were used in this study.

Liposome preparation and high-pressure freezing

Phosphatidylcholine (18:1 (Δ9-Cis) PC), phosphatidylethanolamine (18:1 (Δ9-Cis) PE), phosphatidylserine (18:1 (Δ9-Cis) PS), phosphatidylinositol (18:1 PI) and phosphoinositides (18:1) were from Avanti Polar Lipids. All liposomes contained 45 mol % PC, 30 mol % PE, 20 mol % PS, and either 5 mol % PI or a phosphoinositide. Solutions of PC, PE, and PS in chloroform and PI or phosphoinositides in chloroform:methanol:H2O:HCl (1N) (20:9:1:0.1) were mixed in the required proportion in amber-color glass vials. To improve phosphoinositide homogenization with other lipids, the chloroform:methanol 2:1 ratio was maintained in the mixture. A lipid film was produced by evaporation of solvents in the vial under the stream of nitrogen gas and then drying using a vacuum desiccator for 2 h. The dried lipid film was stored at -20 °C with argon gas and used within 2 days.

The lipid film was resuspended in a buffer containing 220 mM sucrose and 20 mM HEPES (pH 7.4, adjusted with NaOH). The suspension was vortexed well and then freeze-thawed 5 times in liquid nitrogen and warm water (~60 °C). Unilamellar liposomes were produced by extrusion through a 0.4 µm pore size polycarbonate filter using an extrusion apparatus (Avanti Polar Lipids). After extrusion, the liposomes were diluted 5 times in 120 mM NaCl, 20 mM HEPES buffer (pH 7.4, adjusted with NaOH), and centrifuged for 20 min at 15,000 g. The same amount of 100% glycerol was applied to the pellets of the liposomes as a cryoprotectant. The liposome/glycerol mixture was placed on a copper carrier with a ring of double-sided tape (140-µm thickness), covered with another carrier, and then frozen by a high-pressure freezing machine (HPM010, BAL-TEC). The frozen samples were stored in

liquid nitrogen until use.

High-pressure freezing of acute cerebellar slices

Acute slices of mouse cerebellum were prepared at physiological temperature (PT) as described previously (Eguchi et al., 2020). Briefly, mice were decapitated under isoflurane anesthesia and their brains were quickly removed from the skull and immersed into a cutting solution containing (mM): 300 sucrose, 2.5 KCl, 10 glucose, 1.25 NaH_2PO_4, 2 Na Pyruvate, 3 *myo*-inositol, 0.5 Na ascorbate, 26 $NaHCO_3$, 0.1 $CaCl_2$, 6 $MgCl_2$ (pH 7.4 when gassed with 95% O_2/5% CO_2) at PT (35-37 °C). The cerebellum was dissected from the whole brain and immediately glued on a cutting stage of a tissue slicer (Linear Slicer Pro7, Dosaka EM, Kyoto, Japan) and sliced (sagittal, 140-160 µm thickness) in the cutting solution kept at PT. Slices were then maintained in the artificial cerebrospinal fluid (ACSF) containing (in mM): 125 NaCl, 2.5 KCl, 10 glucose, 1.25 NaH_2PO_4, 2 sodium pyruvate, 3 *myo*-inositol, 0.5 sodium ascorbate, 26 $NaHCO_3$, 2 $CaCl_2$, 1 $MgCl_2$ (pH 7.4 when gassed with 95% O_2/5% CO_2) at 37 °C until use. Small blocks containing lobule IV-VII were trimmed from the slices in the cutting solution using a micro scalpel (#10316-14, FST). The trimmed block was transferred into cryoprotectant buffer (15% polyvinylpyrrolidone in ACSF with 10 mM HEPES, pH 7.3 adjusted with NaOH), sandwiched between two copper carriers with a ring of double-sided tape (140-µm thickness), and then frozen by a high pressure freezing machine. The frozen samples were stored in liquid nitrogen until use.

SDS-digested freeze-fracture replica labeling (SDS-FRL)

The frozen samples were fractured into two parts at -130 °C and replicated by carbon (4-5 nm thick), carbon-platinum (uni-direction from 60°, 2 nm), and carbon (20-25 nm) deposition in a freeze-fracture machine (JFD-V, JOEL, Tokyo, Japan). The samples were digested with

159 2.5% SDS solution containing 0.1 M Tris-HCl (pH 8.3) at 80°C for 18-22 h. The replicas
160 were washed in the SDS solution and then a washing buffer (50 mM Tris-buffered saline
161 (TBS, pH 7.4) containing 0.1% BSA) at RT. To avoid non-specific binding of the probes and
162 antibodies, the replicas were blocked with 3% BSA, 2% cold fish skin gelatin, and 0.05%
163 Tween-20 in TBS for 1 h at RT. The replicas were incubated with 50 ng/ml GST-tagged PH
164 domain of phospholipase C δ1 (PI(4,5)P_2-Grip, Echelon Inc.) in a dilution buffer (1% BSA,
165 1% cold fish skin gelatin, and 0.05% Tween-20 in TBS) at 4°C overnight. Then the replica
166 was incubated with anti-GST antibody (rabbit IgG, 5 µg/ml, Bethyl Laboratories) and anti-
167 $Ca_V2.1$ antibody (guinea pig, 2.5 µg/ml, Synaptic Systems) as a marker of neurons at 15°C
168 overnight, and then gold-nanoparticle conjugated secondary antibodies (goat anti-rabbit IgG,
169 5 nm, 1:50, BBI; donkey anti-guinea pig IgG, 12 nm, 1:30, Jackson Immnoresearch)
170 dissolved in the dilution buffer at 15°C overnight. For double labeling of PI(4,5)P_2 with
171 proteins, the replicas were incubated with a mixture of primary antibodies (GluD2: rabbit
172 anti-GST IgG + guinea pig anti-GluD2 IgG (2.0 µg/ml, Frontier Institute); GIRK3: chicken
173 anti-GST IgY (5 µg/ml, Bethyl Laboratories) + rabbit anti-GIRK3 IgG (XX µg/ml, Frontier
174 Institute); mGluR1α: rabbit anti-GST IgG + guinea pig anti-mGluR1α IgG (XX µg/ml,
175 Frontier Institute)) at 15°C 1-2 overnight and then with gold-nanoparticle conjugated
176 secondary antibodies at 15°C overnight. After washing the replicas with the washing buffer,
177 they were picked up onto a grid coated with formvar in distilled water. Images were obtained
178 under TEM (Tecnai 10) with RADIUS software at magnifications of 65,000 and 39,000.
179

180 **Image analysis**

181 Images were analyzed with Darea software (Kleindienst et al., 2020), Fiji, and R. The gold
182 particle detection and the demarcation of the region of interest were performed on Darea
183 software. AZs on the P-face of PF boutons were indicated with the aggregation of

184 intramembrane particles on the replica at the electron microscopic level as described
185 previously (Eguchi et al., 2022, 2020; Harris and Landis, 1986; Landis and Reese, 1974;
186 Masugi-Tokita et al., 2007). Gold particles inside or < 30 nm away from the demarcation
187 border of AZs (outer rim) were counted as the particles in the AZs (Kleindienst et al., 2020).
188 Because the PSD area on the P-face of dendritic spines of PCs cannot be identified based on
189 morphological features, the largest cluster of GluD2-labeling gold particles on the spines was
190 identified as the PSD area (Eguchi et al., 2020; Luján et al., 2018a). The demarcated region
191 of the images was imported to R via FIJI/ImageJ for the following point pattern analysis.
192 Point pattern analysis of the gold particles described below was performed using spatstat
193 package (version 2.3-0) of R (version 4.1.0). Nearest neighbor distances (NNDs) to both
194 particles of the same size (e.g. from a 5 nm particle to the nearest 5 nm particle) and the other
195 size (e.g. from a 5 nm particle to the nearest 10 nm particle) were computed to evaluate the
196 distribution pattern of the particles. Center Periphery Index (CPI), indicating the location of
197 the particles in the AZs or PSDs, was calculated as the square of the normalized distances
198 from the center of the region of interest. When particles are randomly distributed in a circle,
199 the mean CPI is near 0.5 (Kleindienst et al., 2020). To assess the randomness of the particle
200 distribution, we performed two types of Monte-Carlo simulations, termed random and fitted
201 simulations, following the methods described in the previous publications (Kleindienst et al.,
202 2020; Luján et al., 2018b) using R. For the random simulation, particles were randomly
203 placed on the demarcated area. The simulated particles were placed to keep the minimum
204 distance of 10 nm from any other particles and then randomly shifted within a disc with a 30-
205 nm diameter to reproduce the immunolabeling with a probe and antibodies (Tabata et al.,
206 2019). In the fitted simulation, a constraint was added that the distance distribution between
207 the simulated particles should not differ significantly from the distance distribution between
208 the original particles. The particle distribution pattern was modeled and simulated as a

Matern Cluster point process, and the goodness-of-fit between the real and simulated distribution was assessed by comparing both the all pairwise distances (APD) and NNDs of the particles using the two-sample *Kolmogorov-Smirnov* test (KS test), respectively, and considered them similar if the p-value was equal or above 0.1 for both. To avoid excessive statistical power due to the large sample size caused by a large number of particles, parametric bootstrapping was performed when the number of values to be compared exceeded 100. Specifically, we first randomly selected 100 distance values (NND or APD) from the simulated distribution and compared them to the empirical cumulative distribution function of the distance values of the real distribution using the KS test. This process was repeated 1,000 times, and the average of the p-values was used to assess the goodness-of-fit. Gold particle clusters were detected with a hierarchical clustering algorithm called Ward linkage (Figure S1) and a density-based clustering algorithm called DBSCAN (Figures 2 and 3). For Ward linkage, the threshold distance was set as 50 nm. For DBSCAN, we set the minimum number of particles consisting of a cluster as 3 and the maximum distance between particles as the sum of the median and 1.5 times the interquartile range (IQR) of the NNDs. The area of the convex polygon connecting the outermost particles forming the cluster was defined as the cluster area.

Statistical analysis

To consider the hierarchical structure, correlation, and probability distribution, data were analyzed with either a linear mixed-effects model (LMM) or its generalized form (GLMM) using the lme4 package (version 1.1-27.1) of R (Aarts et al., 2014; Yu et al., 2021). Probability distributions for models were chosen by the goodness of fit to Poisson (for discrete variables e.g. the number of particles), normal (e.g. CPI), or gamma distribution (for continuous variables e.g. NNDs). Appropriate to the particular experiment and statistical

model, fixation methods (perfusion- and cryo-fixation), the faces of cell membranes (P- and E-face), components of neurons (e.g. somata, spines, AZs on PF boutons), genotypes (wildtype and Ts65Dn), and potentially their interactions were used as fixed effects, while experiments, animals, replicas, and cells were used as random effects to consider the nested and/or crossed data structure in the statistical analysis. For all experiments, at least four animals per condition were used. All data are presented as estimated marginal means with 95% confidence intervals (CI, in figures) or standard error of means (s.e.m., in text) estimated using the emmeans package. The goodness-of-fit of the models was assessed by second-order Akaike Information Criterion (AICc) for the elimination of the random factors (MuMIn package and then by likelihood ratio chi-square tests (Chi-LRT) with models in which the fixed effects of interest had been dropped. For multiple pairwise comparisons between 3 or more groups, posthoc comparisons to assume the significance of differences between pairs of group means were performed using emmeans packages with Tukey (for all pairwise) or Benjamini-Hochberg (BH, for selected pairwise) method when Chi-LRT detected a significant difference ($p < 0.05$). Statistical significance was assumed if $p < 0.05$ (indicated with blue or single asterisk), $p < 0.01$ (green or double asterisk), and $p < 0.001$ (red or triple asterisk).

Results

Visualization of nanoscale PI(4,5)P_2 distribution on SDS-digested freeze-fracture replica preparations of mouse brain tissues

To observe the nanoscale two-dimensional distribution of PI(4,5)P_2, SDS-FRL has been utilized on cultured human fibroblasts, mouse smooth muscle cells, and rat pancreatic exocrine acinar cells (Fujita et al., 2009; Ozato-Sakurai et al., 2011). In this study, we

259 optimized this method for mouse cerebellar tissues to quantitatively analyze the nanoscale
260 PI(4,5)P_2 distribution on neuronal cell membranes. We used a recombinant GST-tagged PH
261 domain of PLCδ1 (GST-PH) as a specific probe of PI(4,5)P_2. To verify the specificity of
262 GST-PH among the PI stereoisomers, we labeled freeze-fracture replicas of liposomes
263 containing either PhdIns or a PI stereoisomer (5 mol%) with GST-PH (50 ng/ml), anti-GST
264 primary antibody, and gold particle-conjugated secondary antibody. The density of
265 immunogold particles was much higher on the replica prepared from PI(4,5)P_2 liposome
266 compared to those from other liposomes (Figure 1A), indicating a high specificity of the
267 PI(4,5)P_2 probe (Figure 1B).
268 To visualize the two-dimensional (2D) distribution of PI(4,5)P_2 on neuronal cell membranes,
269 we labeled PI(4,5)P_2 in the mouse cerebellum using SDS-FRL with GST-PH. Acute slices
270 prepared at physiological temperature (Eguchi et al., 2020) were frozen under high pressure
271 with 15% PVP as a cryoprotectant (Figure 1C) to minimize damage caused by ice crystals
272 during freezing (Borges-Merjane et al., 2020). After the SDS-digestion to remove cytosolic
273 proteins and extracellular matrix, cerebellar replicas were sequentially incubated with GST-
274 PH, primary antibodies, and gold particle-conjugated secondary antibodies. $Ca_V2.1$ was co-
275 labeled using an anti-$Ca_V2.1$ antibody directed against its intracellular domain (Althof et al.,
276 2015), giving specific labeling on the cytoplasmic leaflets (P-face) of neuronal cell
277 membranes. Immunogold particles that label PI(4,5)P_2 by GST-PH (PI(4,5)P_2 particles)
278 showed higher density on the P-face of the somatic membrane of Purkinje cells (PCs) than on
279 the E-face (Chi-square likelihood-ratio test (Chi-LRT): $p < 0.001$; Figures 1D and 1E),
280 indicating the dominance of PI(4,5)P_2 distribution on the cytoplasmic leaflet of the cell
281 membranes. The particle density without GST-PH was significantly lower on both E- and P-
282 face of the PC somatic membranes than that with GST-PH (Figures S1A and S1B), indicating
283 that even the low-density PI(4,5)P_2 labeling on the E-face is ascribable to GST-PH binding.

284 To quantitatively investigate whether PI(4,5)P_2 is clustered on somatic membranes of PCs,
285 we performed Monte-Caro random simulations and compared the nearest neighbor distance
286 (NND) between the observed and simulated PI(4,5)P_2 particles from all images (Szoboszlay
287 et al., 2017). The mean NNDs of the observed PI(4,5)P_2 particles were around half of the
288 simulated one (Chi-LRT: $p < 0.001$, Figure 1F), indicating clustering of PI(4,5)P_2 on the
289 membrane. The distribution of NNDs between PI(4,5)P_2 particles obtained from a PC somatic
290 membrane (Figure 1G) is highly right-skewed (skewness = 3.55). Fitting this distribution
291 with Gaussian mixture modeling shows that the NNDs between PI(4,5)P_2 particles are
292 produced from a mixture of short and long NND populations. These results indicate that
293 PI(4,5)P_2 on the PC soma has two distinct distribution patterns, clustered and scattered, and
294 that most PI(4,5)P_2 constitute clusters (Figure 1G). The PI(4,5)P_2 particle clusters were also
295 observed on the E-face of the somatic membrane (Figure S1C). The number of particles in a
296 cluster was significantly lower without GST-PH than that with GST-PH on both E- and P-
297 face (Figure S1C). These results indicate that PI(4,5)P_2 forms clusters on both the outer and
298 inner leaflets of the somatic membranes.
299 To examine whether the density of PI(4,5)P_2 differs between neuronal cell types in the
300 cerebellum, we observed somatic membranes of cerebellar granule cells (GCs) and molecular
301 layer interneurons (MLIs). PI(4,5)P_2 particles were also distributed on the P-face making
302 clusters in somatic membranes of both cell types (Figure 1H). Although the density of
303 PI(4,5)P_2 particles in the somatic membrane of GCs was significantly higher than that of
304 MLIs (multiple pairwise comparisons with Tukey adjustment (Tukey): $p < 0.001$; Figure 1I),
305 the NNDs of the PI(4,5)P_2 particles on somatic membranes of the cerebellar neurons did not
306 differ between the cell types (Chi-LRT: $p = 0.12$; Figure 1J), indicating a similar local
307 concentration of PI(4,5)P_2 in these clusters across the examined cerebellar neuronal cell
308 types.

309

310 **PI(4,5)P_2 distribution on somatodendritic compartments of PCs**

311 We next investigate whether the distribution of PI(4,5)P_2 differs among somatodendritic
312 compartments of PCs: somata, main shafts (MS), smooth branchlets (SmB), spiny branchlets
313 (SpB), and spines. EM pictures of each dendritic component were taken in the molecular
314 layer (ML) divided into proximal (MS), intermediate (SmB) and distal one-third (SpB,
315 spines) of the PC layer. Gold particles for PI(4,5)P_2 were observed throughout all the
316 dendritic compartments (Figure 2A). The density of PI(4,5)P_2 particles was found to increase
317 gradually from the proximal to the distal dendrites (Chi-LRT: $p < 0.001$; Figure 2B): spine
318 membranes showed a ~1.5 times higher density of PI(4,5)P_2 particles than somatic, MS, and
319 SmB membranes (Tukey: $p < 0.001$), whereas no significant difference compared to SpB
320 membranes was detected (Tukey: $p = 0.43$). Mean NNDs of PI(4,5)P_2 particles were not
321 significantly different between the compartments (Figure 2B, Chi-LRT: $p = 0.55$), indicating
322 that the local concentration of PI(4,5)P_2 does not differ between different somatodendritic
323 compartments of PCs.

324 PI(4,5)P_2 particles on the dendritic membranes formed clusters as seen on the somatic
325 membranes. To quantitatively compare the PI(4,5)P_2 cluster profiles (cluster area, particle
326 number in cluster, and intra-cluster density) between all compartments of somatodendritic
327 membranes, we detected the clusters using the Density-Based Spatial Clustering of
328 Applications with Noise (DBSCAN) algorithm (Methods, (Szoboszlay et al., 2017). The
329 DBSCAN detected variable sizes of PI(4,5)P_2 particle clusters on the somatodendritic
330 membranes (Figure 2C). The density of PI(4,5)P_2 clusters on the PC cell membranes
331 gradually increased from the proximal to the distal compartments (Chi-LRT: $p < 0.001$;
332 Figure 2D); spine membranes showed a higher density of PI(4,5)P_2 clusters than somatic,
333 MS, and SmB membranes (Tukey: $p < 0.001$), whereas no significant difference with SpB

334 membranes was detected (Tukey: $p = 0.21$). The cluster area was not significantly different
335 between all compartments of somatodendritic membranes (Chi-LRT: $p = 0.10$; Figure 2D),
336 whereas intra-cluster $PI(4,5)P_2$ particle density in spines was significantly higher than those
337 in other compartments (Chi-LRT: $p < 0.001$; Figure 2D). These results suggest that $PI(4,5)P_2$
338 are distributed throughout all compartments of somatodendritic membranes of PCs, and the
339 density is higher at the distal dendrites and spines than at the soma and proximal dendrites.
340 This proximo-distal gradient of $PI(4,5)P_2$ along the somatodendritic compartments of PC
341 membranes is ascribable to an increase in the density of $PI(4,5)P_2$ clusters rather than the
342 cluster size, and a higher $PI(4,5)P_2$ density within clusters on spine membranes.
343
344 **$PI(4,5)P_2$ distribution on membrane compartments of GCs and MLIs**
345 We next examined the $PI(4,5)P_2$ distributions in different compartments of GCs (somata,
346 dendrites, parallel fiber (PF) axons, presynaptic PF boutons with PC spines (PF-PC) or MLI
347 dendrites (PF-MLI)) and MLIs (somata, dendrites, presynaptic basket cell boutons on PC
348 somata (BC-PC)). Gold particles for $PI(4,5)P_2$ were observed throughout all compartments of
349 GCs and MLIs (Figures 3A and 3B). In the GC membranes, the density of $PI(4,5)P_2$ particles
350 was not significantly different between the compartments (Chi-LRT: $p = 0.095$; Figure 3C),
351 though the mean NNDs of $PI(4,5)P_2$ particles were slightly but significantly different
352 between somatic and axonal membranes (Tukey: $p = 0.027$, Figure 3C). The cluster
353 parameters of $PI(4,5)P_2$ were also not significantly different between the compartments
354 (Figure 3D). These results suggest that $PI(4,5)P_2$ in GC membranes shows a similar
355 distribution pattern throughout the subcellular compartments.
356 In MLIs, the $PI(4,5)P_2$ density was not significantly different between the membrane
357 compartments, but the mean NNDs were larger in dendritic and presynaptic bouton
358 membranes than in somatic membranes (Figure 3E). This difference is caused by larger

359 population of scattered PI(4,5)P_2 in these compartments as shown in Figure S2. The intra-
360 cluster density of PI(4,5)P_2 in the bouton membrane was significantly higher than in the
361 somatic membrane, whereas the cluster density and area were similar between the
362 compartments (Figure 3F).
363
364 **PI(4,5)P_2 distribution on synaptic membranes**
365 Next, we focused on PI(4,5)P_2 distribution in the presynaptic membrane of PF (Figure 4A).
366 Since many presynaptic proteins related to neurotransmitter release contain PI(4,5)P_2-binding
367 domains (Martin, 2001), PI(4,5)P_2 is expected to be localized at the presynaptic active zones
368 (AZs). The PI(4,5)P_2 particle density was significantly higher in the AZs than in the whole
369 bouton and extra-AZ membranes at both PF-PC and PF-MLI synapses (Tukey: $p < 0.001$;
370 Figure 4B). The observed density of PI(4,5)P_2 particles in AZs was significantly higher than
371 that of randomly distributed PI(4,5)P_2 particles on the bouton membrane by Monte-Carlo
372 simulation (Chi-LRT: $p < 0.001$ (PF-PC) and $p = 0.002$ (PF-MLI); Figure 4C). Next, we
373 examined how the PI(4,5)P_2 particles are distributed within the AZs using the center-
374 periphery index (CPI), where a CPI of 0 indicates that the particle is at the center of gravity,
375 and a CPI of 1 indicates the particle is at the edge of the AZ (Kleindienst et al., 2020). The
376 histogram of CPI in the bouton membranes suggests that the particles are distributed at a high
377 density within the AZ and that the distribution probability decreases with distance from the
378 AZ (Figure 4D, top). The CPI of the particles within AZs was higher at around CPI = 1.0
379 compared to the values of the random simulation (Figure 4D, bottom), indicating that
380 PI(4,5)P_2 is preferentially located in the periphery of the AZs. The mean CPI of the PI(4,5)P_2
381 particles in AZs was significantly higher than that of randomly distributed particles (Chi-
382 LRT: $p < 0.001$, Figure 4E) in both PF-PC and PF-MLI synapses. These results suggest that
383 AZ, in particular, its periphery is PI(4,5)P_2-enriched regardless of postsynaptic cell types.

384 Next, we investigated the PI(4,5)P_2 distribution in PSD of dendritic spines. The PI(4,5)P_2
385 particles were distributed throughout the spine membranes (Figure 4F), and the density in the
386 PSDs was not significantly different compared to the whole spine and extra-PSD membranes
387 (Chi-LRT: p = 0.77; Figure 4G). The observed PI(4,5)P_2 particle density in PSDs was not
388 significantly higher than that of the particles randomly distributed in the spine (Chi-LRT: p =
389 0.25; Figure 4H). Furthermore, the CPI of the PI(4,5)P_2 particles in the spines was uniformly
390 distributed, and the CPI in the PSDs was similar to the simulated particles randomly
391 distributed (Figure 4I). These results suggest that PI(4,5)P_2 is not specifically accumulated in
392 the postsynaptic site of PC dendritic spines.
393
394 **The association of ion channels and receptors with PI(4,5)P_2 on cell membranes of**
395 **cerebellar neurons**
396 *The association of Ca_V2.1 with PI(4,5)P_2*
397 Ca_V2.1 is an α-subunit of P/Q-type voltage-gated calcium channels and is regulated by
398 PI(4,5)P_2 directly or indirectly through Ca_V β-subunit (Suh et al., 2012; Suh and Hille, 2008).
399 Here, we examined whether Ca_V2.1 is associated with PI(4,5)P_2 in the neuronal membranes
400 by co-immunolabeling of Ca_V2.1 with the PI(4,5)P_2 labeling. To assess the association, we
401 compared NNDs from Ca_V2.1 to PI(4,5)P_2 particles ($NND_{C\text{-}P}$) between observed and
402 simulated Ca_V2.1 particles. To reproduce the Ca_V2.1 clustering in the simulation, we
403 performed a fitted simulation of Ca_V2.1 particle distribution (Methods, (Kleindienst et al.,
404 2020; Luján et al., 2018b)). In PCs, Ca_V2.1 is broadly expressed in somatodendritic
405 membranes (Figure 5A) as previously reported (Indriati et al, 2013). The real values of
406 $NND_{C\text{-}P}$ in somatic, SpB, and spine membranes were significantly shorter than the simulated
407 ones (Figure 5B). The mean $NND_{C\text{-}P}$ was not significantly different between the
408 compartments of PC membranes (Figure 5C). In GCs, Ca_V2.1 was highly expressed in

409 somatic and presynaptic AZ membranes (Figure 5D). The comparison of NND_{C-P} between
410 observed and simulated $Ca_V2.1$ particles showed significant differences in the somatic and
411 PF-PC/MLI AZ membranes (Figure 5E), indicating the association of $Ca_V2.1$ with $PI(4,5)P_2$.
412 The mean NND_{C-P} values in PF-PC and PF-MLI AZs were not significantly different (Figure
413 5F). In MLI, $Ca_V2.1$ was expressed in somatic and presynaptic basket cell (BC)-PC bouton
414 membranes (Figure 6A). The NND_{C-P} in somatic and BC-PC bouton membranes was
415 significantly shorter than the simulated one (Figure 6B). These results suggest the ubiquitous
416 association of $Ca_V2.1$ with $PI(4,5)P_2$ in neuronal cell membranes across various cell types
417 and their compartments.
418
419 *The association of GIRK3 channels with $PI(4,5)P_2$*
420 $PI(4,5)P_2$ is associated with some ion channels and regulates their activities, e.g., open
421 channel probability (Suh and Hille, 2008). G protein-coupled inwardly rectifying K^+ (GIRK)
422 channels are a family of lipid-gated potassium channels that are activated by $PI(4,5)P_2$ and G-
423 protein βγ-subunits ($G_{\beta\gamma}$) released from G-protein coupled receptors (GPCRs) (Whorton and
424 MacKinnon, 2011). Thus, GIRK channels are expected to be associated with $PI(4,5)P_2$
425 clusters in order to be efficiently activated. To examine whether $PI(4,5)P_2$ and GIRK
426 channels are co-clustered on dendritic membranes of mouse cerebellar PCs, we co-labeled
427 $PI(4,5)P_2$ and GIRK3, the most predominant subunit of GIRK channels in PCs (Aguado et al.,
428 2008; Fernández-Alacid et al., 2009), on the P-face of the dendritic membranes. The GIRK3
429 particles were observed throughout the dendritic SpBs and spines of the PCs (Figure 7A). We
430 compared the NNDs from GIRK3 to $PI(4,5)P_2$ particles (NND_{G-P}) between observed and
431 simulated GIRK3 particles in spines and SpBs spines of PCs. The real NND_{G-P} in both spines
432 and SpBs was significantly shorter than the simulated one (Chi-LRT: $p < 0.001$, Figure 7B),
433 suggesting that GIRK3 channels co-clustered with $PI(4,5)P_2$ in the distal dendritic

434 membranes of PCs. GIRK channels are also expressed on presynaptic PF-PC boutons,
435 including AZs (Figure 7A, (Fernández-Alacid et al., 2009; Luján et al., 2018b), and may
436 regulate presynaptic excitability. In the presynaptic AZs, the real NND_{G-P} was significantly
437 shorter than the simulated one (Chi-LRT: $p < 0.001$, Figure 7B), indicating the coexistence of
438 GIRK3 with $PI(4,5)P_2$. The mean NND_{G-P} in spine and AZ membranes was significantly
439 shorter than that in SpB membranes (Figure 7C), suggesting the tighter association of GIRK3
440 and $PI(4,5)P_2$ in synaptic membranes.
441
442 *The association of mGluR1α with $PI(4,5)P_2$*
443 Group I metabotropic glutamate receptors (mGluRs) are GPCRs coupled with $G\alpha_q$ subunit
444 and hydrolyze $PI(4,5)P_2$ into inositol 1,4,5-trisphosphate (IP_3) and diacylglycerol (DAG)
445 through the activation of PLCβ. A subtype of Group I mGluRs mGluR1α is highly expressed
446 on the dendritic shafts and spines but avoids PSDs in PCs, and forms clusters (Luján et al.,
447 2018a). To effectively produce the second messengers from $PI(4,5)P_2$, a mGluR1α cluster is
448 expected to be located close to the $PI(4,5)P_2$ clusters on the dendritic membrane of PCs. To
449 address this possibility, we co-labeled mGluR1α with $PI(4,5)P_2$ on the dendritic membranes
450 of PCs and compared the NNDs between mGluR1α and $PI(4,5)P_2$ particles (NND_{M-P}) with
451 the fitted simulation of the mGluR1α particle distribution. The mGluR1α particles were
452 distributed as clusters on the membranes of spines and SpBs (Figure 7D-E) as previously
453 reported (Luján et al., 2018a). The real NND_{M-P} was significantly shorter than the simulated
454 one on the spine membrane (Chi-LRT: $p < 0.001$) but not on the SpB membrane (Chi-LRT: p
455 = 0.36, Figure 7F). These results suggest compartment-specific co-clustering of mGluR1α
456 with $PI(4,5)P_2$ on PC spines.
457

458 **Discussion**

459 **Visualization of PI(4,5)P_2 distribution on neuronal cell membranes using SDS-FRL**

460 To understand how and where PI(4,5)P_2 exerts the physiological functions in neurons, it is
461 essential to know its nanoscale distribution in the neuronal cell membranes. To visualize the
462 distribution of PI(4,5)P_2 on the cell membrane, cryofixation of phospholipids is necessary
463 because they diffuse laterally even after chemical fixation (Tanaka et al., 2010). Detergents
464 and organic solvents used in conventional immunoEM methods disrupt the cell membrane
465 and should be avoided. In regions with densely packed proteins such as AZs and PSDs,
466 limited accessibility of the probes could hamper quantitative analysis of the PI(4,5)P_2
467 distribution. The fluorescent protein-tagged PH domain of PLCδ1 has been developed as a
468 specific probe for PI(4,5)P_2 (Idevall-Hagren and De Camilli, 2015). This probe allows us to
469 perform single-molecule imaging of PI(4,5)P_2 on the plasma membrane of the cultured cells
470 using super-resolution microscopies such as Stimulated Emission Depletion (STED)
471 microscopy and Direct Stochastic Optical Reconstruction Microscopy (dSTORM)
472 (Milovanovic et al., 2016; Wang and Richards, 2012). However, it is still difficult to observe
473 the PI(4,5)P_2 distribution on neuronal cell membranes in brain tissues because of the limited
474 accessibility of the probes in AZs and PSDs. In addition, overexpressed fluorescent probes
475 interfere with endogenous protein binding to PI(4,5)P_2 by masking PI(4,5)P_2 on the cell
476 membrane (Suh and Hille, 2008), making it difficult to quantify the changes in PI(4,5)P_2.
477 Thus, the SDS-FRL with cryo-fixed brain tissue used in this study has the advantage of
478 visualizing accurately the native PI(4,5)P_2 distribution. In this method, phospholipids are
479 physically immobilized by high-pressure freezing and replication by deposition of evaporated
480 carbon/platinum, so the phospholipids do not diffuse after freezing. Since cytosolic proteins
481 are removed by SDS treatment, PI(4,5)P_2 and transmembrane proteins are exposed on the
482 replica surface, making high accessibility of the probes and antibodies. Due to a low temporal

483 resolution, it is still challenging to examine the dynamics of PI(4,5)P_2 during neuronal
484 activity, but it is a beneficial method to study the nanoscale distribution of PI(4,5)P_2 and
485 other phospholipids on neuronal cell membranes.
486 This study demonstrates that PI(4,5)P_2 is broadly distributed on neuronal cell membranes in
487 the mouse cerebellum. Comparisons of the PI(4,5)P_2 distribution between cell types revealed
488 slightly different densities of PI(4,5)P_2 particles on the somatic membrane, but the differences
489 in distribution patterns between subcellular compartments were more pronounced; in PCs, the
490 PI(4,5)P_2 density was higher at the distal dendrites than at the somatic and proximal
491 dendrites; in GCs, the density was similar at the somata, dendrites, axons, and presynaptic
492 boutons; in MLIs, the density of PI(4,5)P_2 in clusters was lower in presynaptic bouton
493 membranes than somatic and dendritic membranes. These differences in the PI(4,5)P_2
494 distribution patterns may reflect different roles of PI(4,5)P_2 in cell functions between
495 different cell types.
496
497 **PI(4,5)P_2 makes clusters on neuronal cell membranes in mouse cerebellum**
498 Previous studies using super-resolution microscopy have demonstrated that PI(4,5)P_2 forms
499 clusters of 50-100 nm in diameter on the cell membrane, as shown in PC12 cells (Aoyagi et
500 al., 2005; van den Bogaart et al., 2011; Wang and Richards, 2012) and mouse myoblast cells
501 (Petersen et al., 2016). Our study reveals that PI(4,5)P_2 forms clusters of around 1,000 nm^2
502 (corresponding to 35 nm in diameter) on the cell membrane of neurons in the acute cerebellar
503 tissues. The area of the clusters showed almost the same mean values in the somatodendritic
504 and axonal membranes of different neuronal cell types in the cerebellum. The cluster density
505 and the intra-cluster particle density of PI(4,5)P_2 in the PC spine membrane are higher than in
506 other somatodendritic compartments. These observations suggest the accumulation of
507 densely-packed PI(4,5)P_2 clusters in the spine membranes, supporting the contribution of

508 PI(4,5)P_2 and other PIs to spine formation and morphological long-term plasticity (Lei et al.,
509 2017; Ueda and Hayashi, 2013). Although it is still unknown why PI(4,5)P_2 forms clusters,
510 the clustered PI(4,5)P_2 localization indicates the importance of a close spatial relationship
511 between the clusters and effector proteins for their effective interaction, as discussed in the
512 following section.
513
514 **PI(4,5)P_2 distribution in the synaptic membrane**
515 In this study, we found the accumulation of PI(4,5)P_2 in AZ membranes of the presynaptic PF
516 boutons regardless of the postsynaptic cell types. This result suggests the roles of PI(4,5)P_2
517 on presynaptic activities, including vesicle exocytosis and endocytosis. At the presynaptic
518 membrane, Rab6-interacting proteins (RIMs) have PI(4,5)P_2-binding sites at C2A and C2B
519 domains, and their interactions are essential for efficient exocytosis (de Jong et al., 2018).
520 PI(4,5)P_2 also interacts with a SNARE protein syntaxin-1A and an SV Ca^{2+} sensor protein
521 synaptotagmin-1 (Aoyagi et al., 2005; Honigmann et al., 2013; Milovanovic et al., 2016).
522 Since $Ca_V2.1$ directly binds to RIMs and dominantly induces Ca^{2+} influx into PF boutons, the
523 association of $Ca_V2.1$ with PI(4,5)P_2 supports the idea that PI(4,5)P_2 anchors SVs and Ca^{2+}
524 channels through interaction with these proteins. PI(4,5)P_2 also regulates vesicle endocytosis
525 via interactions with endocytic proteins e.g., AP-2, AP180, clathrin, and dynamin (Haucke,
526 2005; Martin, 2001; Posor et al., 2015). At calyx of Held synapses of rat brainstem,
527 upregulation of PI(4,5)P_2 by the retrograde signals through the nitric oxide/cyclic GMP-
528 activated protein kinase/RhoA/Rho-associated protein kinase pathway accelerates vesicle
529 endocytosis, which strengthens the homeostatic plasticity for the maintenance of high-
530 frequency synaptic transmission (Eguchi et al., 2012; Taoufiq et al., 2013). PI(4,5)P_2 clusters
531 may work as anchors of presynaptic proteins involved in this pathway providing a site for
532 their interactions.

533

534 **Co-clustering of PI(4,5)P_2 and ion channels and receptors**

535 PI(4,5)P_2 regulates ion channels such as inwardly rectifying K^+ channels, KCNQ channels,
536 transient receptor potential (TRP) channels, and voltage-gated Ca^{2+} channels (Suh and Hille,
537 2008). Therefore, clarifying the distance relationship between these ion channels and
538 PI(4,5)P_2 may provide insight into the regulation mechanism of neuronal excitability by
539 PI(4,5)P_2. In this study, we found that GIRK3 was associated with PI(4,5)P_2 in SpB and
540 spines of PCs and also AZs of PF boutons. Because PI(4,5)P_2 is essential to activate GIRK
541 channels by βγ subunit of G protein (Whorton and MacKinnon, 2011), the association
542 between GIRK3 and PI(4,5)P_2 suggests that GIRK3 on SpB and spines is constantly ready to
543 be activated by G-protein coupled receptors. Since GIRK channels are also associated with
544 $GABA_B$ receptors at different compartments of the cerebellar neurons, such as dendritic
545 shafts and spines of PCs and AZs of PF boutons (Fernández-Alacid et al., 2009; Luján et al.,
546 2018b), the co-assembly of PI(4,5)P_2, GIRK channels and $GABA_B$ receptors may contribute
547 to effective inhibitory postsynaptic transmission on Purkinje cells (Luján et al., 2018b).
548 Group I mGluRs are GPCRs coupled with $G\alpha_q$ subunit and hydrolyze PI(4,5)P_2 into inositol
549 1,4,5-trisphosphate (IP_3) and diacylglycerol (DAG) through the activation of PLCβ. PCs
550 express mGluR1α, a subtype of Group I mGluRs, on the dendritic shafts and spines
551 concentrated in the peri-PSD areas (Luján et al., 2018a). We found a significant association
552 of mGluR1α with PI(4,5)P_2 clusters specific to the spine membrane in PCs, which may
553 contribute to the effective production of the second messengers from PI(4,5)P_2 in response to
554 the glutamate release from presynaptic PF boutons. On the other hand, no particular
555 concentration of PI(4,5)P_2 has been found in the peri-PSD areas. The diffusion dynamics of
556 PI(4,5)P_2 on the spine membrane may be enough to support the interaction with mGluR1α.
557 Thus, the tight spatial association of PI(4,5)P_2 as observed for $Ca_V2.1$ and GIRK3 may not be

558 necessary for the coupling of mGluR1α activation and intracellular signal cascade, though the
559 distance between mGluR1α (and the coupled PLCβ) and PI(4,5)P_2 may affect the kinetics of
560 the second messenger (IP_3 and DAG) production from PI(4,5)P_2.
561
562 The present study demonstrated that the SDS-FRL method could be successfully applied to
563 neuronal cells in acute mouse brain tissues to visualize the distribution of PI(4,5)P_2. We
564 quantitatively analyzed the nanoscale two-dimensional distribution of PI(4,5)P_2 on the cell
565 membrane of mouse cerebellar neurons, and its spatial relationship with GIRK3, Ca_V2.1, and
566 mGluR1α in PC dendrites and PF boutons. Notably, we have demonstrated a higher density
567 of PI(4,5)P_2 in distal PC dendrites, showing a specific association of mGluR1α with PI(4,5)P_2
568 in spines. PI(4,5)P_2 also showed concentration and association with Ca_V2.1 and GIRK3 in
569 presynaptic PF AZs. These results will help to elucidate the physiological functions of
570 PI(4,5)P_2 in neuronal activities, including SV fusion and retrieval in presynaptic membranes
571 and long-term plasticity in postsynaptic spine membranes. This method could also be a
572 powerful tool for the analysis of other PIs and phospholipid distribution in neuronal cell
573 membranes using specific probes.
574
575 **Author Contributions**
576 KE and RS designed and conducted the experiments and wrote the manuscript. KE analyzed
577 the data.
578
579
580

581 **References**

582 Aarts E, Verhage M, Veenvliet JV, Dolan CV, Van Der Sluis S. 2014. A solution to
583 dependency: Using multilevel analysis to accommodate nested data. *Nature Neuroscience*.
584 doi:10.1038/nn.3648

585 Aguado C, Colón J, Ciruela F, Schlaudraff F, Cabañero MJ, Perry C, Watanabe M, Liss B,
586 Wickman K, Luján R. 2008. Cell type-specific subunit composition of G protein-gated
587 potassium channels in the cerebellum. *J Neurochem* **105**:497–511.

588 Aktar S, Takatori S, Tsuji T, Orii M, Ohsaki Y, Cheng J, Fujimoto T. 2017. A New Electron
589 Microscopic Method to Observe the Distribution of Phosphatidylinositol 3,4-bisphosphate.
590 *Acta Histochem Cytochem* **50**:141–147.

591 Althof D, Baehrens D, Watanabe M, Suzuki N, Fakler B, Kulik Á. 2015. Inhibitory and
592 excitatory axon terminals share a common nano-architecture of their Cav2.1 (P/Q-type)
593 Ca(2+) channels. *Front Cell Neurosci* **9**:315.

594 Aoyagi K, Sugaya T, Umeda M, Yamamoto S, Terakawa S, Takahashi M. 2005. The
595 activation of exocytotic sites by the formation of phosphatidylinositol 4,5-bisphosphate
596 microdomains at syntaxin clusters. *J Biol Chem* **280**:17346–17352.

597 Borges-Merjane C, Kim O, Jonas P. 2020. Functional Electron Microscopy, "Flash and
598 Freeze," of Identified Cortical Synapses in Acute Brain Slices. *Neuron* **105**:992–1006.e6.

599 Cheng J, Fujita A, Yamamoto H, Tatematsu T, Kakuta S, Obara K, Ohsumi Y, Fujimoto T.
600 2014. Yeast and mammalian autophagosomes exhibit distinct phosphatidylinositol 3-
601 phosphate asymmetries. *Nat Commun* **5**. doi:10.1038/ncomms4207

602 de Jong APH, Roggero CM, Ho MR, Wong MY, Brautigam CA, Rizo J, Kaeser PS. 2018.

603 RIM C2B Domains Target Presynaptic Active Zone Functions to PIP2-Containing
604 Membranes. *Neuron* **98**:335–349.e7.

605 Di Paolo G, De Camilli P. 2006. Phosphoinositides in cell regulation and membrane
606 dynamics. *Nature* **443**:651–657.

607 Eguchi K, Montanaro J, Le Monnier E, Shigemoto R. 2022. The Number and Distinct
608 Clustering Patterns of Voltage-Gated Calcium Channels in Nerve Terminals. *Front*
609 *Neuroanat* **16**. doi:10.3389/fnana.2022.846615

610 Eguchi K, Nakanishi S, Takagi H, Taoufiq Z, Takahashi T. 2012. Maturation of a PKG-
611 Dependent Retrograde Mechanism for Exoendocytic Coupling of Synaptic Vesicles. *Neuron*
612 **74**:517–529.

613 Eguchi K, Velicky P, Hollergschwandtner E, Itakura M, Fukazawa Y, Danzl JG, Shigemoto
614 R. 2020. Advantages of Acute Brain Slices Prepared at Physiological Temperature in the
615 Characterization of Synaptic Functions. *Front Cell Neurosci* **14**:63.

616 Falkenburger BH, Jensen JB, Dickson EJ, Suh BC, Hille B. 2010. Phosphoinositides: Lipid
617 regulators of membrane proteins. *J Physiol* **588**:3179–3185.

618 Fernández-Alacid L, Aguado C, Ciruela F, Martín R, Colón J, Cabañero MJ, Gassmann M,
619 Watanabe M, Shigemoto R, Wickman K, Bettler B, Sánchez-Prieto J, Luján R. 2009.
620 Subcellular compartment-specific molecular diversity of pre- and post-synaptic GABA-
621 activated GIRK channels in Purkinje cells: Pre- and post-synaptic GABAB-activated GIRK
622 channels in PCs. *J Neurochem* **110**:1363–1376.

623 Fujita A, Cheng J, Tauchi-Sato K, Takenawa T, Fujimoto T. 2009. A distinct pool of
624 phosphatidylinositol 4,5-bisphosphate in caveolae revealed by a nanoscale labeling
625 technique. *Proc Natl Acad Sci U S A* **106**:9256–9261.

626 Harris KM, Landis DM. 1986. Membrane structure at synaptic junctions in area CA1 of the
627 rat hippocampus. *Neuroscience* **19**:857–872.

628 Haucke V. 2005. Phosphoinositide regulation of clathrin-mediated endocytosis. *Biochem Soc*
629 *Trans* **33**:1285–1289.

630 Honigmann A, van den Bogaart G, Iraheta E, Risselada HJ, Milovanovic D, Mueller V,
631 Müllar S, Diederichsen U, Fasshauer D, Grubmüller H, Hell SW, Eggeling C, Kühnel K,
632 Jahn R. 2013. Phosphatidylinositol 4,5-bisphosphate clusters act as molecular beacons for
633 vesicle recruitment. *Nat Struct Mol Biol* **20**:679–686.

634 Idevall-Hagren O, De Camilli P. 2015. Detection and manipulation of phosphoinositides.
635 *Biochim Biophys Acta* **1851**:736–745.

636 Kleindienst D, Montanaro J, Bhandari P, Case MJ, Fukazawa Y, Shigemoto R. 2020. Deep
637 Learning-Assisted High-Throughput Analysis of Freeze-Fracture Replica Images Applied to
638 Glutamate Receptors and Calcium Channels at Hippocampal Synapses. *Int J Mol Sci* **21**.
639 doi:10.3390/ijms21186737

640 Landis DM, Reese TS. 1974. Differences in membrane structure between excitatory and
641 inhibitory synapses in the cerebellar cortex. *J Comp Neurol* **155**:93–125.

642 Lei W, Myers KR, Rui Y, Hladyshau S, Tsygankov D, Zheng JQ. 2017. Phosphoinositide-
643 dependent enrichment of actin monomers in dendritic spines regulates synapse development
644 and plasticity. *J Cell Biol* **216**:2551–2564.

645 Luján R, Aguado C, Ciruela F, Arus XM, Martín-Belmonte A, Alfaro-Ruiz R, Martínez-
646 Gómez J, de la Ossa L, Watanabe M, Adelman JP, Shigemoto R, Fukazawa Y. 2018a. SK2
647 Channels Associate With mGlu1α Receptors and CaV2.1 Channels in Purkinje Cells. *Front*
648 *Cell Neurosci* **12**:311.

649 Luján R, Aguado C, Ciruela F, Cózar J, Kleindienst D, de la Ossa L, Bettler B, Wickman K,
650 Watanabe M, Shigemoto R, Fukazawa Y. 2018b. Differential association of GABAB
651 receptors with their effector ion channels in Purkinje cells. *Brain Struct Funct* **223**:1565–
652 1587.

653 Maekawa M, Fairn GD. 2014. Molecular probes to visualize the location, organization and
654 dynamics of lipids. *J Cell Sci* **127**:4801–4812.

655 Martin TFJ. 2001. PI(4,5) P2 regulation of surface membrane traffic. *Curr Opin Cell Biol*
656 **13**:493–499.

657 Masugi-Tokita M, Tarusawa E, Watanabe M, Molnar E, Fujimoto K, Shigemoto R. 2007.
658 Number and Density of AMPA Receptors in Individual Synapses in the Rat Cerebellum as
659 Revealed by SDS-Digested Freeze-Fracture Replica Labeling. *Journal of Neuroscience*
660 **27**:2135–2144.

661 Milovanovic D, Platen M, Junius M, Diederichsen U, Schaap IAT, Honigmann A, Jahn R,
662 Van Den Bogaart G. 2016. Calcium promotes the formation of syntaxin 1 mesoscale domains
663 through phosphatidylinositol 4,5-bisphosphate. *J Biol Chem* **291**:7868–7876.

664 Ozato-Sakurai N, Fujita A, Fujimoto T. 2011. The distribution of phosphatidylinositol 4,5-
665 bisphosphate in acinar cells of rat pancreas revealed with the Freeze-Fracture replica labeling
666 method. *PLoS One* **6**. doi:10.1371/journal.pone.0023567

667 Petersen EN, Chung H-W, Nayebosadri A, Hansen SB. 2016. Kinetic disruption of lipid rafts
668 is a mechanosensor for phospholipase D. *Nat Commun* **7**:13873.

669 Posor Y, Eichhorn-Grünig M, Haucke V. 2015. Phosphoinositides in endocytosis. *Biochimica*
670 *et Biophysica Acta - Molecular and Cell Biology of Lipids* **1851**:794–804.

671 Suh B-C, Hille B. 2008. PIP2 is a necessary cofactor for ion channel function: how and why?
672 *Annu Rev Biophys* **37**:175–195.

673 Suh B-C, Kim D-I, Falkenburger BH, Hille B. 2012. Membrane-localized -subunits alter the
674 PIP2 regulation of high-voltage activated Ca2+ channels. *Proceedings of the National*
675 *Academy of Sciences* **109**:3161–3166.

676 Szoboszlay M, Kirizs T, Nusser Z. 2017. Objective quantification of nanoscale protein
677 distributions. *Sci Rep* **7**:15240.

678 Tabata S, Jevtic M, Kurashige N, Fuchida H, Kido M, Tani K, Zenmyo N, Uchinomiya S,
679 Harada H, Itakura M, Hamachi I, Shigemoto R, Ojida A. 2019. Electron Microscopic
680 Detection of Single Membrane Proteins by a Specific Chemical Labeling. *iScience* **22**:256–
681 268.

682 Tanaka KAK, Suzuki KGN, Shirai YM, Shibutani ST, Miyahara MSH, Tsuboi H, Yahara M,
683 Yoshimura A, Mayor S, Fujiwara TK, Kusumi A. 2010. Membrane molecules mobile even
684 after chemical fixation. *Nat Methods* **7**:865–866.

685 Taoufiq Z, Eguchi K, Takahashi T. 2013. Rho-Kinase Accelerates Synaptic Vesicle
686 Endocytosis by Linking Cyclic GMP-Dependent Protein Kinase Activity to
687 Phosphatidylinositol-4,5-Bisphosphate Synthesis. *Journal of Neuroscience* **33**:12099–12104.

688 Tsuji T, Takatori S, Fujimoto T. 2019. Definition of phosphoinositide distribution in the
689 nanoscale. *Current Opinion in Cell Biology*. doi:10.1016/j.ceb.2018.10.008

690 Ueda Y, Hayashi Y. 2013. PIP3 Regulates Spinule Formation in Dendritic Spines during
691 Structural Long-Term Potentiation. *Journal of Neuroscience* **33**:11040–11047.

692 van den Bogaart G, Meyenberg K, Risselada HJ, Amin H, Willig KI, Hubrich BE, Dier M,

Hell SW, Grubmüller H, Diederichsen U, Jahn R. 2011. Membrane protein sequestering by ionic protein-lipid interactions. *Nature* **479**:552–555.

Wang J, Richards DA. 2012. Segregation of PIP2 and PIP3 into distinct nanoscale regions within the plasma membrane. *Biol Open* **1**:857–862.

Wenk MR, De Camilli P. 2004. Protein-lipid interactions and phosphoinositide metabolism in membrane traffic: Insights from vesicle recycling in nerve terminals. *Proceedings of the National Academy of Sciences* **101**:8262–8269.

Whorton MR, MacKinnon R. 2011. Crystal structure of the mammalian GIRK2 K+ channel and gating regulation by G proteins, PIP2, and sodium. *Cell* **147**:199–208.

Yu Z, Guindani M, Grieco SF, Chen L, Holmes TC, Xu X. 2021. Beyond t test and ANOVA: applications of mixed-effects models for more rigorous statistical analysis in neuroscience research. *Neuron*. doi:10.1016/j.neuron.2021.10.030

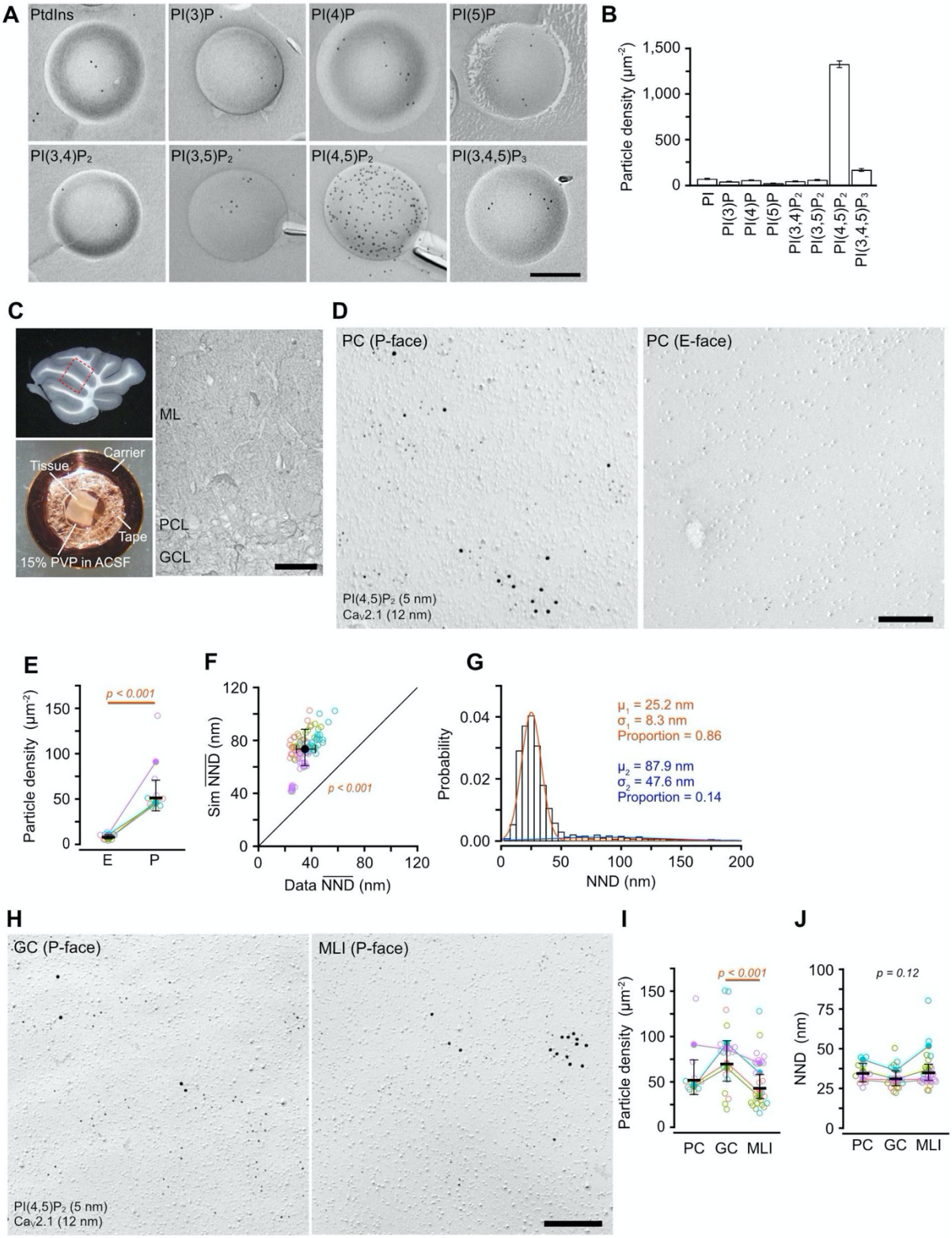

707

708 **Figure 1. SDS-FRL of PI(4,5)P_2 on somatic membranes of mouse cerebellar neurons.**

709 (**A-B**) Specificity of PI(4,5)P_2 labeling. Replicas of liposomes containing 5% PtdIns or

710 different stereoisomers of PIs were labeled using GST-PH, anti-GST antibody, and 5-nm gold
711 particle-conjugated secondary antibody (**A**, Scale bar = 200 nm). The density of gold
712 particles was highest in the liposome containing PI(4,5)P_2 (**B**).

713 (**C**) Acute cerebellar slice preparation for high-pressure freezing (HPF) and replica
714 preparation. Left-top, an acute sagittal slice of the mouse cerebellum. The dashed line
715 indicates the trimmed region for HPF. Left-bottom, a trimmed cerebellar slice on a copper
716 carrier with double-sided tape for HPF. Right, low-magnification transmission electron
717 microscopic (TEM) image of the mouse cerebellar replica containing granule cell layer
718 (GCL), Purkinje cell layer (PCL), and molecular layer (ML). Scale bar = 20 μm.

719 (**D**) Example TEM image of 5-nm gold particle labeling for PI(4,5)P_2 with immunogold
720 labeling for $Ca_V2.1$ (12 nm) on P- (left) and E-face (right) of the PC somatic membranes of
721 cerebellar PC. Scale bar = 200 nm.

722 (**E**) Statistical comparison of the PI(4,5)P_2 particle density on the E-face and P-face of the PC
723 somatic membranes. Open and closed circles indicate the means of the PI(4,5)P_2 particle
724 density in each PC and each mouse, respectively, with different colors. Black horizontal bars
725 indicate estimated marginal means (emmeans, thick bars) and 95% confidence intervals (CIs,
726 error bars) of the density estimated by GLMM (Methods). The PI(4,5)P_2 density was
727 significantly higher on the P-face than on the E-face of the PC somatic membranes (P-face:
728 51.2 ± 8.5 particles/μm^2, E-face: 8.0 ± 1.2 particles/μm^2, n = 213 images/12 cells/4 mice, $p <$
729 0.001, Chi-square likelihood ratio test (Chi-LRT)).

730 (**F**) Comparison of nearest neighbor distances (NND) between real (Data NND, x-axis) and
731 simulated (Sim NND, y-axis) PI(4,5)P_2 particles on PC somatic membranes. Data-NNDs are
732 significantly smaller than Sim NNDs (Data: 35.1 ± 3.6 nm, Sim: 73.3 ± 7.0 nm, n = 206
733 images/11 cells/4 mice, $p < 0.001$, Chi-LRT).

(**G**) Distribution of NNDs of the PI(4,5)P_2 particles obtained from a single PC somatic membrane (n = 2,929 particles). Red and blue lines indicate the distinct components of the NND distribution estimated from the Gaussian mixture modeling.

(**H**) PI(4,5)P_2 labeling (5 nm) with $Ca_V2.1$ (12 nm) on the P-face of GC (left) and molecular layer interneuron (MLI, right) somatic membranes. Scale bar = 200 nm.

(**I**) The PI(4,5)P_2 particle density on the somatic membranes (P-face) of different neuronal cell types in the mouse cerebellum (PC: 51.8 ± 9.6 particles/μm^2, GC: 69.8 ± 11.3 particles/μm^2, MLI: 42.9 ± 6.7 particles/μm^2, n = 273 images/57 cells/4 mice, p = 0.003, Chi-LRT).

(**J**) NND of the PI(4,5)P_2 particles on the somatic membranes of different neuronal cell types in the mouse cerebellum (PC: 34.4 ± 3.0 nm, GC: 31.0 ± 2.4 nm, MLI: 34.8 ± 2.6 nm, n = 65,607 values/57 cells/4 mice, p = 0.12, Chi-LRT).

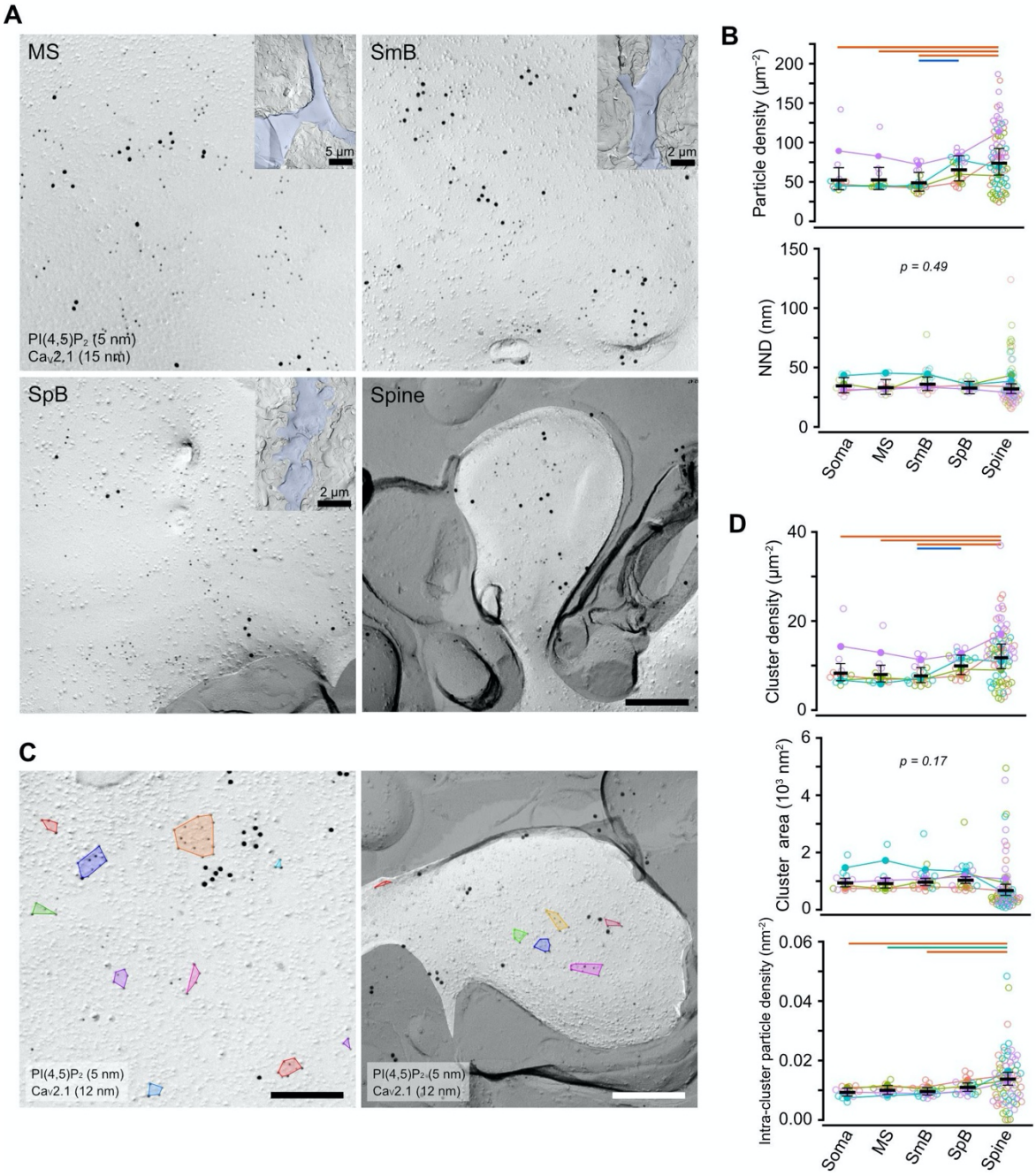

Figure 2. PI(4,5)P_2 particle distribution on somatodendritic membranes of PCs.

(**A**) Example images obtained from the different compartments of PC dendritic membranes: main shaft (MS, top-left), smooth branchlet (SmB, top-right), spiny branchlet (SpB, bottom-left), and spine (bottom-right). Scale bar = 200 nm. Inset: low-magnification images of MS, SmB, and SpB, respectively, indicated with blue.

753 (**B**) Comparison of the PI(4,5)P_2 particle density (top) and NNDs (bottom) in the
754 somatodendritic membrane compartments of PCs. The PI(4,5)P_2 density gradually increased
755 from soma and proximal dendrites to distal dendritic components (top, n = 611 images/134
756 components/4 mice, $p < 0.001$, Chi-LRT), whereas no significant difference in NNDs was
757 detected between these compartments (bottom, n = 67,380 values/134 components/4 mice, p
758 = 0.49, Chi-LRT).

759 (**C**) Example images of the PI(4,5)P_2 clusters on the somatic (left) and spine (right)
760 membrane of PCs. Colored polygons indicate individual PI(4,5)P_2 clusters detected by the
761 DBSCAN algorithm. Scale bars = 200 nm.

762 (**D**) Quantitative analysis of the PI(4,5)P_2 clusters on the somatodendritic compartments of
763 PCs. Top, the number of clusters per area (cluster density, n = 611 values/134 components/4
764 mice). Middle, the cluster area (10,479 clusters/124 components/4 mice). Bottom, the intra-
765 cluster particle density (10,343 clusters/134 components/4 mice). The cluster density and the
766 intra-cluster particle density are significantly higher in spine membranes compared to the
767 somatic and proximal dendritic membranes ($p < 0.001$, Chi-LRT), whereas there is no
768 significant difference in the cluster area (p = 0.17, Chi-LRT).

769

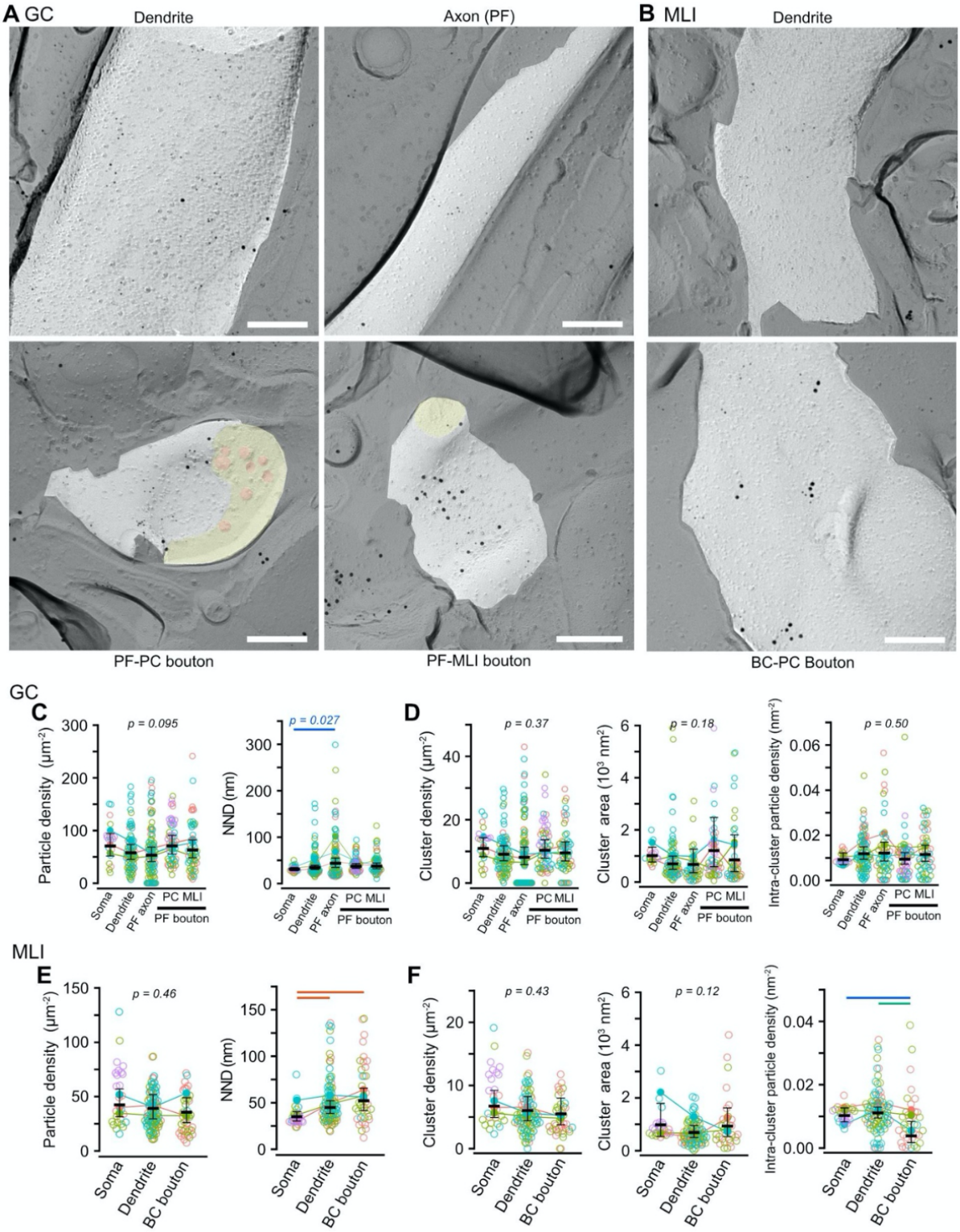

Figure 3. PI(4,5)P_2 particle distribution in GCs and MLIs.

(**A**) Example images obtained from the different compartments of GC membranes: dendrites (top-left), parallel fiber (PF) axons (top-right), presynaptic PF boutons on the PC spine (PC-

774 PF, bottom-left) and on the MLI dendrite (PF-MLI, bottom-right). Yellow and orange in the
775 PF boutons indicate the cross-fracture and synaptic vesicle membranes, respectively. Scale
776 bars = 200 nm.

777 (**B**) Example images obtained from different compartments of MLI membranes: dendrites
778 (top) and basket cell (BC) presynaptic bouton on PC soma (bottom). Scale bar = 200 nm.

779 (**C**) Comparison of the PI(4,5)P_2 particle density (left) and NNDs (right) in the different GC
780 membrane compartments. NNDs show significant differences between the compartments (n =
781 67,380 values/134 components/4 mice, $p < 0.001$, Chi-LRT), whereas there is no significance
782 in the density (n = 376 images/320 components/4 mice, p = 0.09, Chi-LRT).

783 (**D**) Quantitative analysis of the PI(4,5)P_2 particle clusters in different GC membrane
784 compartments. There are no significant differences in the cluster density (n = 376 images/320
785 components/4 mice, p = 0.37, Chi-LRT), the cluster area (n = 4070 clusters/254
786 components/4 mice, p = 0.18, Chi-LRT), and the intra-cluster particle density (n = 4004
787 clusters/253 compartments/4 mice, p = 0.50, Chi-LRT).

788 (**E**) Comparison of the PI(4,5)P_2 particle density (left) and NNDs (right) in different
789 membrane compartments of MLIs. NNDs in dendritic and BC bouton membranes are
790 significantly larger than that in somatic membranes (n = 24,012 values/152 components/4
791 mice, $p < 0.001$, Chi-LRT), whereas there is no significant difference in the density between
792 the compartments (n = 230 images/153 components/4 mice, p = 0.46, Chi-LRT).

793 (**F**) Quantitative analysis of the PI(4,5)P_2 particle clusters in different MLI membrane
794 compartments. The intra-cluster particle density in BC bouton membranes is significantly
795 smaller than the other components (n = 3,766 clusters/149 components/4 mice, p = 0.03, Chi-
796 LRT), whereas no significant difference was detected in the cluster density (n = 230

images/153 components/4 mice, p = 0.43, Chi-LRT) and the cluster area (n = 3,822 clusters/146 components/4 mice, p = 0.12, Chi-LRT) between these compartments.

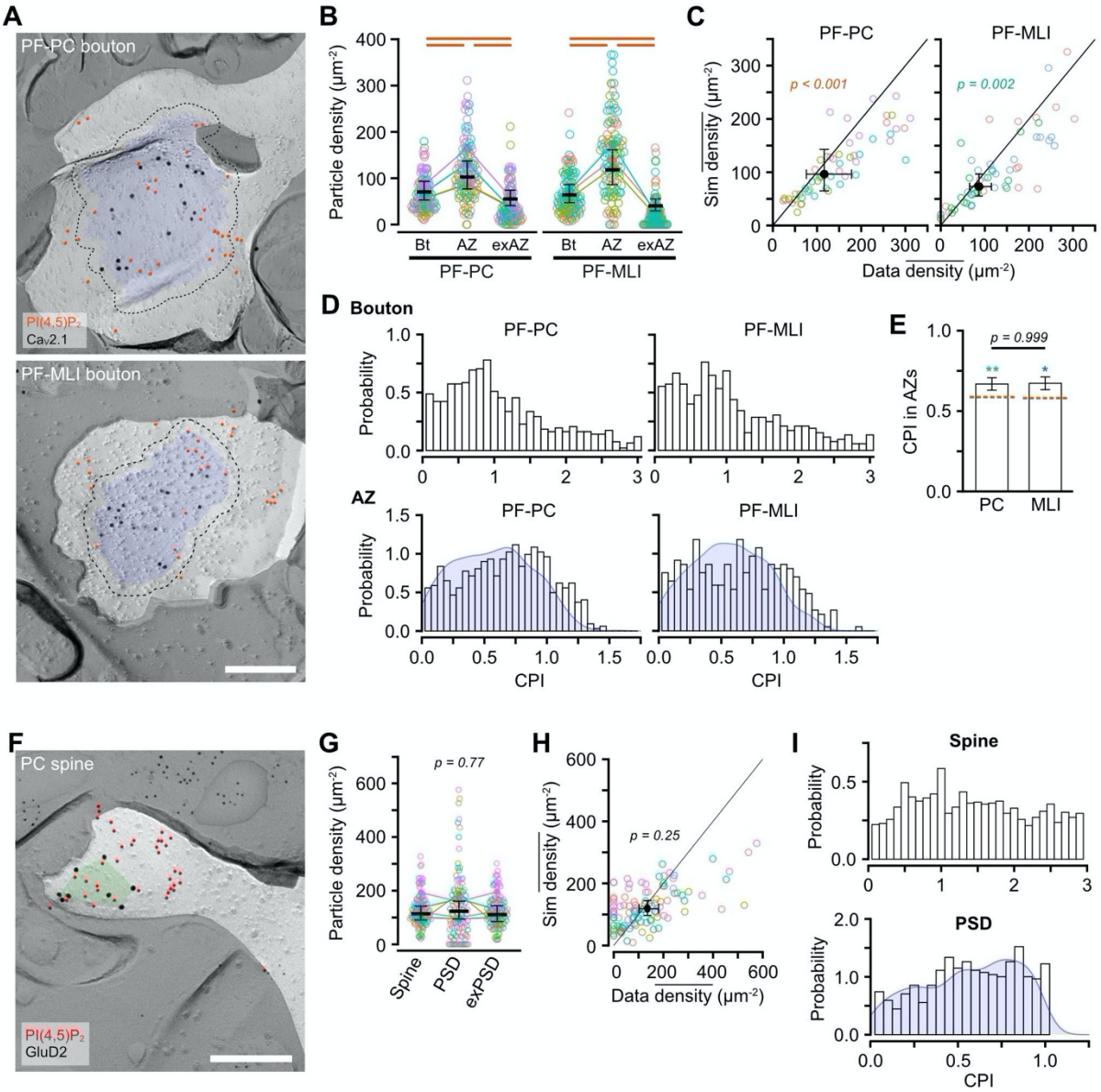

Figure 4. PI(4,5)P_2 distribution in pre- and post-synaptic membranes of PF-PC synapses.

(**A**) Example images for PI(4,5)P_2 particle distribution on the membranes of PF-PC (top) and PF-MLI bouton (bottom). Red and black circles indicate gold particles for PI(4,5)P_2 and

805 $Ca_V2.1$, respectively. The Blue area and dotted line indicate AZ and outer-rim (30 nm from
806 the edge of AZ, Methods), respectively. Scale bar = 200 nm.

807 (**B**) Beeswarm plot of the $PI(4,5)P_2$ density in the whole bouton (Bt), AZs, and extra-AZ
808 region (exAZ) of the PF-PC (left) and PF-MLI (right) bouton membranes. The $PI(4,5)P_2$
809 density was significantly higher in AZs than in the whole bouton and the exAZ in both PF-PC
810 and PF-MLI boutons (n = 111 boutons/4 mice, $p < 0.001$, Tukey method).

811 (**C**) Comparison of the $PI(4,5)P_2$ density in the AZs between real and simulated random
812 distribution on the PF bouton membranes. The density of the real particle distribution was
813 significantly higher than that of the simulated one in both PF-PC (real: 97.2 ± 19.7
814 particles/μm^2, sim: 66.7 ± 13.5 particles/μm^2, n = 55 boutons/4 mice, $p < 0.001$, Chi-LRT)
815 and PF-MLI (real 86.7 ± 12.4 particles/μm^2, sim: 73.2 ± 10.4 particles/μm^2, n = 56 boutons/4
816 mice, $p = 0.002$, Chi-LRT) AZ membranes.

817 (**D**) Distribution of center-periphery index (CPI) of $PI(4,5)P_2$ particles in boutons (top) and
818 AZs (bottom). Blue in the bottom graph indicates the CPI distribution of the simulated
819 particles that are randomly distributed in AZs.

820 (**E**) Comparison of CPIs of the $PI(4,5)P_2$ particles in AZs between PF-PC and PF-MLI AZs.
821 There is no significant difference in the CPIs between PF-PC and PF-MLI AZs (PF-PC: 0.67
822 ± 0.02, PF-MLI: 0.67 ± 0.02, n = 107 boutons/4 mice, $p = 0.999$, Chi-LRT). Dashed lines
823 with red show the mean CPIs of the simulated randomly-distributed particles. Asterisks on
824 the bars indicate statistical differences in CPIs between real and simulated particles (PF-PC:
825 0.59 ± 0.02, PF-MLI: 0.58 ± 0.02, $*p < 0.05$, $**p < 0.01$, Tukey method).

826 (**F**) Example images of the $PI(4,5)P_2$ particle distribution on the PC spine membrane. Red and
827 black circles indicate $PI(4,5)P_2$ and GluD2, respectively. The green area indicates

postsynaptic density (PSD) based on the cluster of GluD2. Scale bar = 200 nm.

(**G**) Beeswarm plot of the PI(4,5)P_2 density in the whole spine (spine), PSD, and extra-PSD region (exPSD) of the PC spine membranes. No significant difference in the density was detected between these compartments (n = 108 spines/6 mice, p = 0.77, Chi-LRT).

(**H**) Comparison of the PI(4,5)P_2 density in the PSDs between real and simulated random distribution on the PC spine membranes. The density of the real and simulated particle distribution was not significantly different (real: 0.59 ± 0.01, sim: 0.55 ± 0.01, n = 108 spines/6 mice, p = 0.25, Chi-LRT).

(**I**) Distribution of CPIs of PI(4,5)P_2 particles in spines (top) and PSDs (bottom). Blue in the bottom graph indicates the CPI distribution of the simulated particles that are randomly distributed in PSDs. The CPI of the PI(4,5)P_2 particles is uniformly distributed in the spines and PSDs, suggesting the random distribution of PI(4,5)P_2.

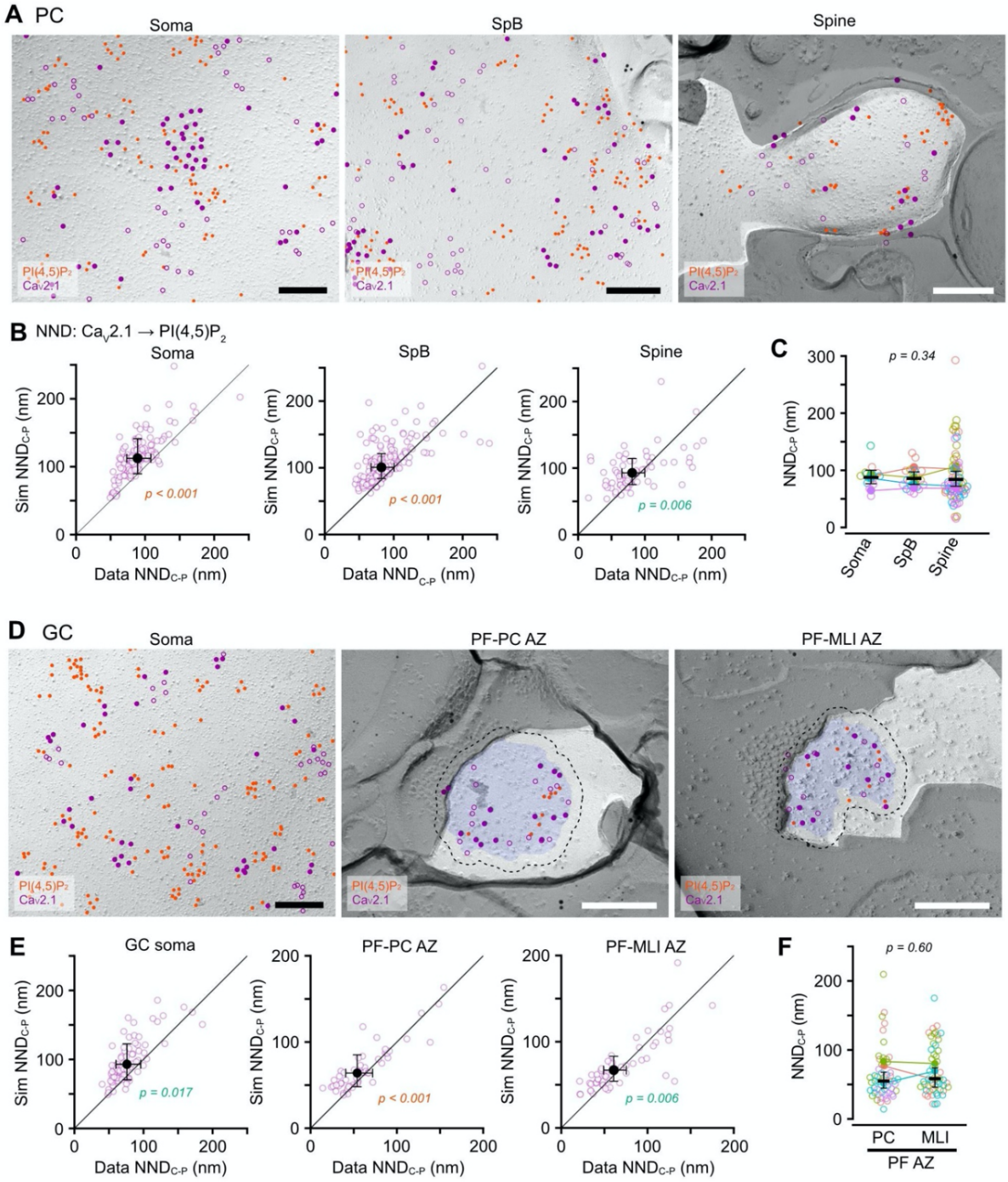

Figure 5. Ubiquitous association of $Ca_V2.1$ with $PI(4,5)P_2$ on cell membranes of PCs and GCs.

(**A**) Example images for co-immunolabeling of $PI(4,5)P_2$ and $Ca_V2.1$ on somatic (left), SpB (middle), and spine (right) membranes of the PC. Red and purple (closed, open) circles indicate $PI(4,5)P_2$ and $Ca_V2.1$ (real, fitted-simulated) particles, respectively. Scale bars = 200

847 nm.

848 (**B**) Comparison of the NNDs from $Ca_V2.1$ to $PI(4,5)P_2$ particles (NND_{C-P}) between real and
849 fitted-simulated $Ca_V2.1$ distribution on somatic (left), SpB (middle), and spine (right)
850 membranes of PCs. The NND_{C-P} of the real distribution was significantly smaller than that of
851 the simulated one in somatic (real: 89.7 ± 9.6 nm, sim: 112.9 ± 12.1 nm, n = 129 images/14
852 cells/5 mice, $p < 0.001$, Chi-LRT), SpB (real: 82.3 ± 8.1 nm, sim: 100.5 ± 9.9 nm, n = 158
853 images/20 dendrites/4 mice, $p < 0.001$, Chi-LRT), and spine membrane (real: 80.9 ± 8.7 nm,
854 sim: 92.8 ± 9.9 nm, 69 spines/4 mice, p = 0.006, Chi-LRT).

855 (**C**) Comparison of NND_{C-P} between somatodendritic compartments. There is no significant
856 difference between the PC compartments (n = 12,956 values/92 components/5 mice, p = 0.70,
857 Chi-LRT).

858 (**D**) Example images for co-immunolabeling of $PI(4,5)P_2$ and $Ca_V2.1$ on somatic (left) and
859 presynaptic PF-PC (middle) and PF-MLI (right) AZ membranes of the GC. Red and purple
860 (closed, open) circles indicate $PI(4,5)P_2$ and $Ca_V2.1$ (real, fitted-simulated) particles,
861 respectively. The Blue area and dotted lines indicate AZs and the outer-rim, respectively.
862 Scale bars = 200 nm.

863 (**E**) Comparison of the NND_{C-P} between real and fitted-simulated $Ca_V2.1$ distribution on
864 somatic (left), PF-PC AZ (middle), and PF-MLI AZ (right) membranes of GCs.The NND_{C-P}
865 of the real distribution was significantly smaller than that of the simulated one in somatic
866 (real: 76.0 ± 9.0 nm, sim: 93.0 ± 13.1 nm, n = 81 images/25 cells/5 mice, p = 0.017, Chi-
867 LRT), PF-PC AZ (real: 54.0 ± 7.9 nm, sim: 64.0 ± 9.3 nm, n = 54 AZs/4 mice, $p < 0.001$,
868 Chi-LRT), and PF-MLI AZ membrane (real: 60.8 ± 6.7 nm, sim: 67.0 ± 7.3 nm, 52 AZs/4
869 mice, p = 0.006, Chi-LRT).

870 (**F**) Comparison of NND_{C-P} between presynaptic AZs of PF-PC and PF-MLI synapses. There
871 is no significant difference in NND_{C-P} between the AZs (n = 1,110 values/68 AZs/4 mice, p =
872 0.60, Chi-LRT).

873

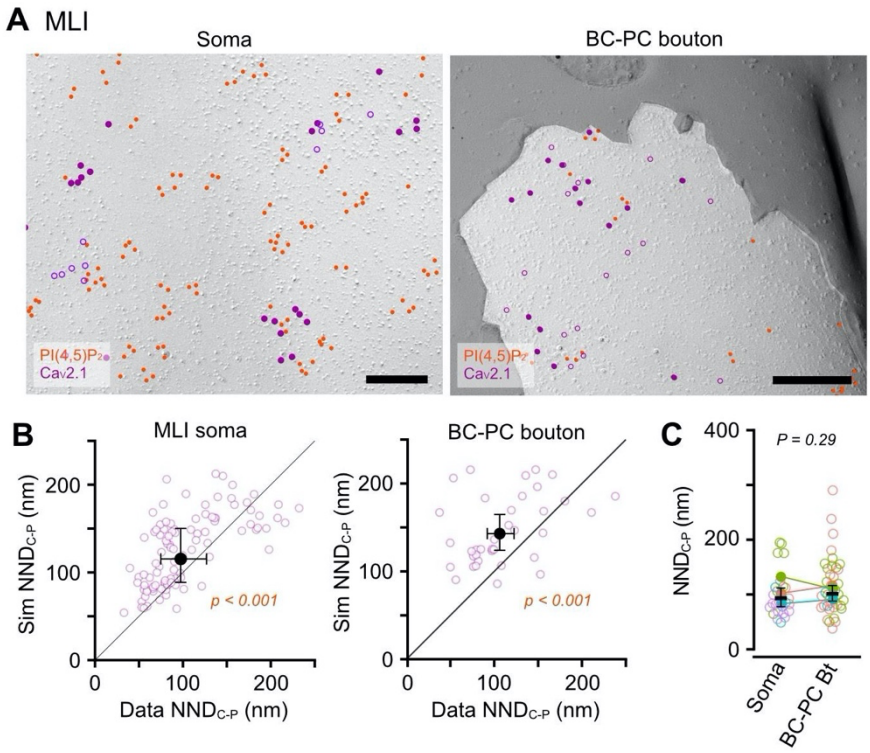

874

875 **Figure 6. Association of $Ca_V2.1$ with $PI(4,5)P_2$ on cell membranes of MLIs.**

876 (**A**) Example images for co-immunolabeling of $PI(4,5)P_2$ and $Ca_V2.1$ on somatic (left) and
877 basket cell (BC)-PC bouton (right) membranes of the MLI. Red and purple (closed, open)
878 circles indicate $PI(4,5)P_2$ and $Ca_V2.1$ (real, fitted-simulated) particles, respectively. P-face of
879 BC-PC boutons were identified based on $Ca_V2.1$ clusters and the surrounding E-face of the
880 PC somatic membranes with $Ca_V2.1$ clusters. Scale bars = 200 nm.

881 (**B**) Comparison of the NND_{C-P} between real and fitted-simulated $Ca_V2.1$ distribution on
882 somatic (left) and BC-PC bouton (right) membranes of MLIs. The NND_{C-P} of the real
883 distribution was significantly smaller than that of the simulated one in somatic (real: 97.5 ±
884 13.1 nm, sim: 115.4 ± 15.5 nm, n = 102 images/26 cells/4 mice, $p < 0.001$, Chi-LRT) and
885 BC-PC bouton membrane (real: 106.0 ± 7.7 nm, sim: 143.0 ± 10.4 nm, 37 boutons/3 mice, p
886 = 0.006, Chi-LRT).

887 (**C**) Comparison of NND_{C-P} between somatic and bouton membranes. No significant

difference was shown between these compartments (n = 2,854 values/63 components/4 mice, $p = 0.29$, Chi-LRT).

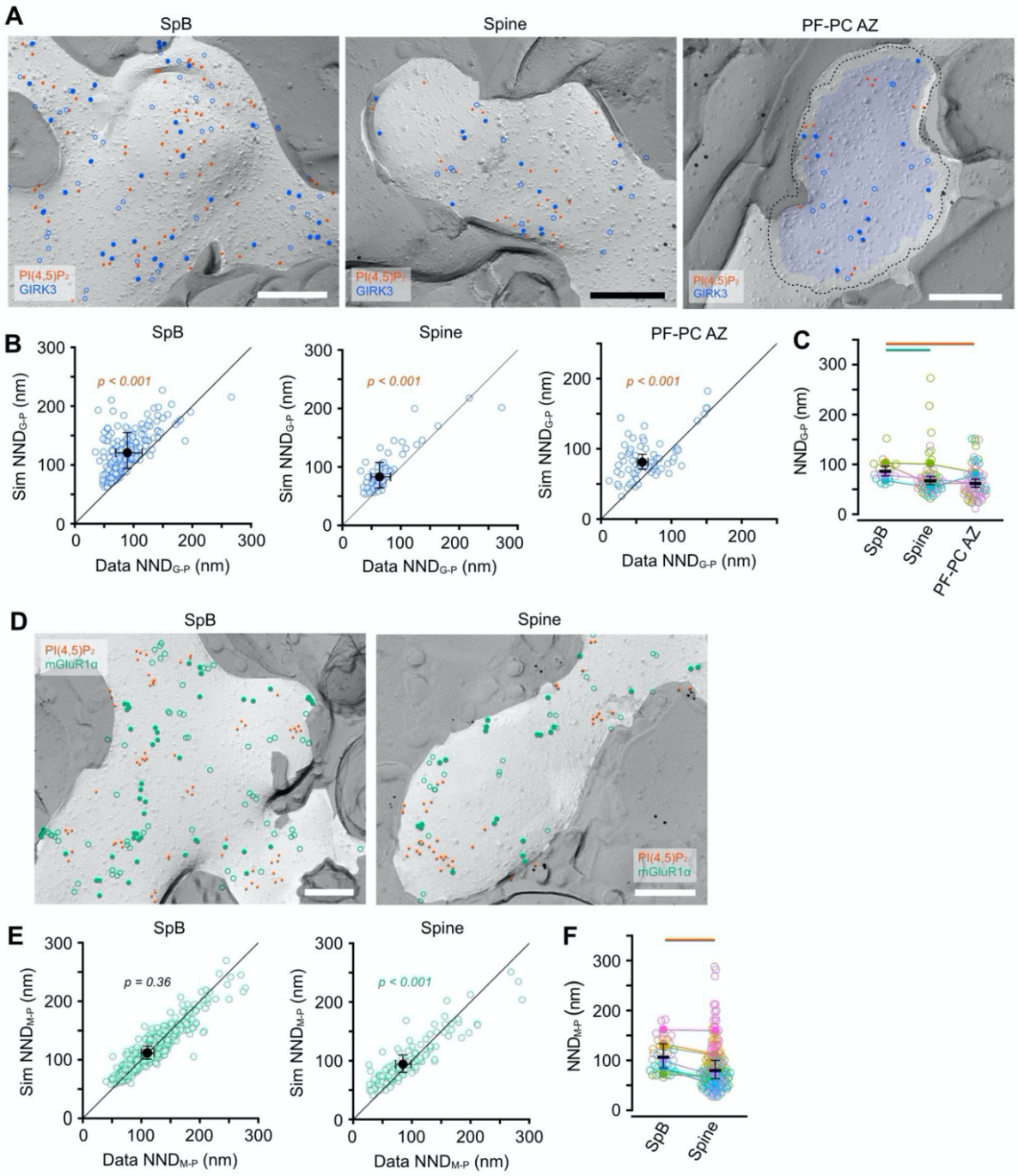

Figure 7. Association of GIRK3 channels and mGluR1α receptors with PI(4,5)P_2 on cell membranes of cerebellar neurons.

(**A**) Example images for co-labeling of PI(4,5)P_2 and GIRK3 channels on PC SpB (left), PC spine (middle), and PF-PC AZ (right) membranes. Red and blue (closed, open) circles indicate PI(4,5)P_2 and GIRK3 (real, fitted-simulated) particles, respectively. The Blue area

897 and a dotted line on the left indicate the AZ and the outer-rim, respectively. Scale bars = 200
898 nm.

899 (**B**) Comparison of the NNDs from GIRK3 to PI(4,5)P_2 particles (NND_{G-P}) between real and
900 fitted-simulated GIRK3 distribution on PC SpB (left), PC spine (middle), and PF-PC AZ
901 (right) membranes. The NND_{G-P} of the real distribution was significantly smaller than that of
902 the simulated one in SpB (real: 89.3 ± 11.4 nm, sim: 120.7 ± 15.4 nm, n = 88 images/19
903 dendrites/5 mice, $p < 0.001$, Chi-LRT), spine (real: 63.6 ± 8.4 nm, sim: 83.0 ± 11.0 nm, n =
904 57 spines/4 mice, $p < 0.001$, Chi-LRT), and PF-PC AZ membrane (real: 58.6 ± 3.9 nm, sim:
905 81.1 ± 5.3 nm, 65 AZs/4 mice, $p < 0.001$, Chi-LRT).

906 (**C**) Comparison of NND_{G-P} between the post- and presynaptic compartments of cerebellar
907 neurons. The NND_{G-P} was significantly shorter in the spine and AZ membranes than in the
908 SpB membrane (4,730 values/90 compartments/4 mice, $p < 0.001$, Chi-LRT).

909 (**D**) Example images for co-labeling of PI(4,5)P_2 and mGluR1α receptors on PC SpB (left)
910 and spine (right) membranes. Red and green (closed, open) circles indicate PI(4,5)P_2 and
911 mGluR1α (real, fitted-simulated) particles, respectively. Scale bars = 200 nm.

912 (**E**) Comparison of the NNDs from mGluR1α to PI(4,5)P_2 particles (NND_{M-P}) between real
913 and fitted-simulated mGluR1α distribution on PC SpB (left) and spine (right) membranes.
914 The NND_{M-P} of the real distribution was significantly smaller than that of the simulated one
915 in the spine membranes (real: 81.8 ± 18.4 nm, sim: 91.2 ± 20.6 nm, n = 140 spines/7 mice, p
916 < 0.001, Chi-LRT), but not in the SpB membrane (n = 147 images/35 dendrites/7 mice, p =
917 0.36, Chi-LRT).

918 (**F**) Comparison of NND_{M-P} between the SpB and spine membranes of PCs. The NND_{M-P} was
919 shorter in the spines than in the SpB membrane (real: 110.0 ± 5.6 nm, sim: 112.0 ± 5.6 nm, n

920 = 22,391 values/140 compartments/7 mice, $p < 0.001$, Chi-LRT).

921